EXTENSION INTO CERAMICS: 3D PRINTING WITH PRECERAMIC POLYMERS

The work in this chapter is based the publication “Analysis of Multi-scale Mechanical Properties of Ceramic Trusses Prepared from Preceramic Polymers" by N.R. Brodnik, J. Schmidt, P. Colombo, and K.T. Faber, which is currently under review in Additive Manufacturing. N.R. Brodnik and J. Schmidt shared first authorship in this work, with N.R. Brodnik taking lead on sample and testing design, and J. Schmidt taking lead on sample fabrication. Both N.R. Brodnik and J. Schmidt contributed to mechanical testing of samples. The details of the print resin and fabrication process used in this study are discussed in reference [1].

0.1 Introduction

In the previous chapter, the potential for designed anisotropy through compliance contrast was demonstrated in a model ceramic system, mica, where stable crack growth can be readily achieved using wedge splitting.[2, 3] While mica is a good ceramic system for stable crack growth coupled with elastic contrast, the possibilities for the introduction of designed anisotropy are relatively limited. To explore greater design possibilities in ceramics, we return to stereolithography as a means to introduce a degree of structural control that cannot be provided by conventional ceramic processing. However, instead of using acrylate photopolymers, we instead use preceramic photopolymers, which can be converted into silicon-based ceramics via pyrolysis.

To date, both stereolithography and digital light processing of preceramic polymer resins have been used to produce a variety of complex structures, and improvements to both the printing and conversion processes indicate there is potential for these systems to begin transitioning into industrial applications.[1, 4–7] However, if preceramic polymer 3D printing, or any other ceramic additive manufacturing technique, is going to prove viable in an industrial setting, it is critical to understand how the complex geometries afforded by 3D printing will affect the properties of the resultant ceramic structure. This effect must be understood both in the context of transformation of the printed part into a ceramic body and in the mechanical response of that ceramic body. Previous analyses on preceramic polymer printing systems across multiple additive manufacturing methods have been restricted to characteristics of the printing resin itself, printing parameters, ceramic yield, and overall linear shrinkage

of representative ceramic bodies.[8–12] In cases where mechanical properties were analyzed, compression tests on bulk structures and flexural tests on representative bodies are most common (e.g. bend beams, discs), and little consideration is given to complex structures.[5, 10, 13–16] Furthermore, even characterization of representative solid bodies is somewhat limited, as the size of bulk structures that can be produced by ceramic additive manufacturing is limited by the available conversion processes, which are diffusion mediated.

In this sense, a mechanical investigation of designed ceramic structures made from printed preceramic polymers can serve two purposes. Not only can stereolithography of preceramic polymers be used to investigate the effects of designed anisotropy, but the introduction of complex design can also be used to better understand the effects of structure on the mechanical properties in printed silicon oxycarbide (SiOC) ceramics, going well beyond what has been explored with simple representative bodies. However, exploration of large bulk structures in this manner is still limited by diffusion-governed ceramic conversion processes. This can be addressed by instead examining lattice structures, which have relatively small solid features, but still demonstrate complex structure at multiple length scales as well as deformation and failure behavior that is structure dependent. The exploration of lattice structures as materials is not a new concept, as many mechanical metamaterials use varieties of interchanging truss structures to tailor elastic deformation behavior at both the macro and micro scales.[17, 18] However, the exploration of interchanging truss structures in the context of failure behavior is not well investigated.

To explore the effect of complex design on ceramics made from printed preceramic polymers, truss structures measuring multiple centimeters in size were printed in different geometric arrangements, and the mechanical properties of not only the pyrolyzed SiOC lattice but also the individual beam elements were analyzed in detail along with the effects of the pyrolysis process on resultant geometry. Two different lattice structures were produced: a Kelvin cell structure which deforms through beam bending, as well as an octet cell structure which deforms through beam stretching. Additionally, to explore the potential for designed anisotropy, a mixed structure was designed to incorporate these two beam configurations within one structure with uniform cell size and stiffness, taking advantage of the possibility to control beam element positioning as well as specific structure deformation modes. If the stiffness can be matched between different truss unit cell elements, it should be possible to create a structure with uniform elastic behavior, but failure strength that varies on

an element by element basis due to differences in deformation, and consequently, failure mode. This would allow for control of fracture behavior at the level of failure strength, and the arrangement of different unit cells in the mixed structure could be used to control the direction of crack propagation.

0.2 Methods

0.2.1 Sample Fabrication

The preceramic printing resin used in this work was based on a selected physical blend of preceramic polymers, discussed in detail by Schmidt and Colombo.[1] The photocurable siloxane TEGO RC 711 (Evonik Industries, Germany) was mixed in equal parts in weight with the high ceramic yield silicone resin H44 (Wacker Chemie A.G., Germany), which was previously dissolved in toluene at a 3/1 weight ratio of solvent/solid polysiloxane. The resin was printed using a digital light processing printer (3DLPrinter-HD 2.0, Robofactory, Italy), which operates in the visible light wavelength range of 400-500 nm. The printed samples were then pyrolyzed in an alumina tube furnace (Carbolite CTF 17/300) at 1000 °C for 1 hour in argon with a temperature ramp of 2 °C/min. During the pyrolysis process, the preceramic polymer blend used in this study exhibits an isotropic linear shrinkage of 51.5 ± 3.3% when measured on representative solid bodies.[1]

Four different structures with overall dimensions of 30 x 30 x 60 mm^3 were designed, each consisting of 7 x 7 x 14 unit cells: two Kelvin cell structures with different beam diameters to explore the effect of aspect ratio in a fixed design, one octet cell structure to explore different deformation modes, and one mixed structure, which combined unit cells from the thick beam Kelvin and octet designs in parallel (see Figure 0.1). Although more complex designs would be desirable to explore, a proof of concept using two different structures in parallel can still demonstrate the potential for matching elastic moduli with different deformation and failure modes. Beam diameters, beam lengths, and unit cell sizes can be seen in Table 0.1. All dimensions listed are for the as-printed state, and all samples in this study will be referenced using their as-printed dimensions, as these were the dimensions that are the most consistent and readily controlled.

0.3 Mechanical Characterization

0.3.1 Print Geometries

Morphological characterization of the printed structures was performed using optical camera (D7500, AF-S Micro Nikkor 40mm Lens, Nikon, Tokyo, Japan), stereo-

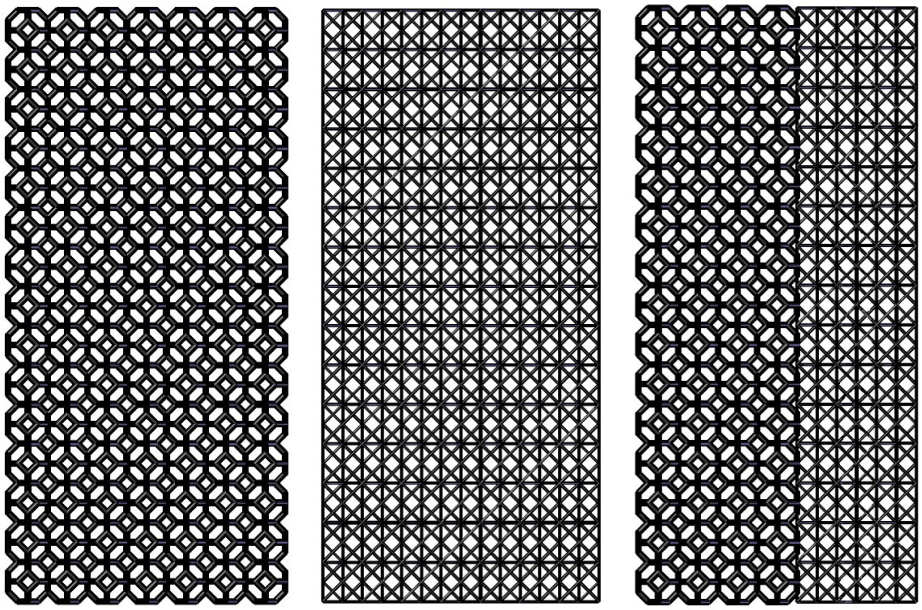

(a) Kelvin Cell Design (b) Octet Cell Design (c) Mixed Cell Design

Figure 0.1: Planar views of the design files for the truss structures investigated. The width of each design is 30 mm and the height is 60 mm.

Table 0.1: Dimensions of as-printed truss designs. Mixed cell designs in this study used a combination of Thick Beam Kelvin Cells and octet Cells.

	Kelvin (Thin Beam)	Kelvin (Thick Beam)	Octet
Beam Diameter (mm)	0.6	0.7	0.34
Beam Length (mm)	1.5	1.5	3.0
Unit Cell Size (mm)	4.2	4.2	4.2

microscopy (STEMI 2000-C, Zeiss, USA), and electron microscopy (Zeiss 1550 VP FE SEM, Carl Zeiss AG, Oberkochen, Germany). To investigate the shrinkages, bulk dimensional values of the structures were measured with a manual digital caliper, while the dimensions of the individual beams were obtained from SEM images analyzed with ImageJ [19] software at several locations.

0.3.2 Truss Structures

To characterize the mechanical properties of the truss systems, two separate sets of mechanical tests were performed: uniaxial compression on entire truss structures, and tensile beam bending (3-point) on individual truss elements. All mechanical tests were performed using an Instron 5982 mechanical testing machine (Instron,

Norwood, MA). Uniaxial compression testing on complete truss structures was done at a constant displacement rate of 0.1 mm/min, to ensure stable quasi-static loading. The elastic moduli of the samples was taken from stress-strain curves of the mechanical compression tests after accounting for fixture compliance.

For uniaxial compression tests, to ensure proper contact over the whole loading area, samples were cut on the top and bottom using a diamond wafering blade in an Isomet 5000 saw (Buehler Inc.). This cut was made through consecutive nodes in the truss system to minimize the occurrence of partial truss cells at the contact surface, which could potentially cause uneven loading or early failure due to contact stresses. In addition to this, to account for load eccentricity, sets of spherical washers were placed on either side of the specimen to allow for a small amount of rotation of load surfaces during compression, as shown in Figure 0.2a.

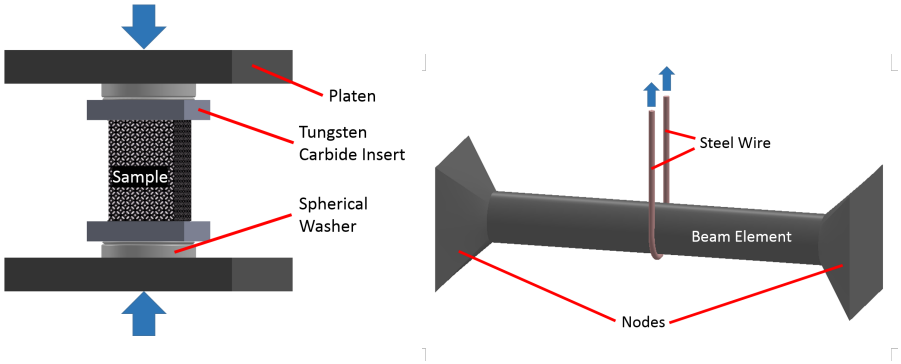

(a) Uniaxial Compression (b) Beam Flexure

Figure 0.2: Schematics of the mechanical tests used to characterize the truss structures in this study.

0.3.3 Beam Elements

For the flexural tests on individual beams, a test setup was adapted from the work by Brezny et al., which investigated the strength of struts in open-cell foams of alumina and zirconia.[20] The truss structures were mounted in a small-scale bench vice and oriented so that the tested beams were arranged horizontally with respect to the loading axis. A low-carbon steel wire with a diameter of 35.56 µm was looped under the center of a single beam and then attached to a tensile fixture on the load frame. This wire was then pulled at a constant displacement rate of 1.0 mm/min to create a tension-driven 3-point bending configuration, as shown in Figure 0.2b.

For flexural testing of individual beam elements, the determination of strength is fairly straightforward. Per ASTM C 1684,[21] the strength of cylindrical rod in

3-point flexure can be described as:

$$\sigma = \frac{8PL}{\pi D^3} \tag{1}$$

where P is the load on the beam (exerted by the wire looped underneath the beam), L is the length of the beam, and D is the diameter. Because this test setup uses a looped wire to apply the bending force, a large amount of compliance is expected during testing. This compliance from the testing fixture made determination of elastic modulus from this test infeasible, as modulus measurement error was too high. Instead, the elastic modulus of the SiOC composing the individual beam elements was established using load controlled nanoindentation with a Berkovich tip as developed by Oliver and Pharr.[**?**]

0.3.4 Analytical Methods for Design of Mixed Structures

Across all mechanical tests, in order for different truss structures to be compared meaningfully, differences in beam geometry and arrangement had to be properly considered. Particularly, in order for truss elements with different deformation modes to be readily interchangeable, the elastic moduli of different unit cells had to match for the same loading conditions. This is best achieved using analytical descriptions of the truss structures, which allow for comparison of failure strengths and elastic moduli for across different densities and beam arrangements. For uniaxial compression tests, all stresses and strains are calculated as engineering stresses and strains using the outer dimensions of the truss structure, including internal porosity. To make these structures mechanically compatible, their effective elastic moduli have to be expressed as a function of beam size and arrangement.

The Kelvin cell structure deforms by bending of beams in the structure that are at a 45° angle with respect to the loading axis. As such, the elastic modulus of the truss structure was determined using calculations developed by Zhu et al. [22] for bending-dominant open cell foams with tetrakaidecahedral (truncated octahedral) cells. For these cell structures, the elastic modulus is equivalent along all axes of the cubic unit cell, and can be expressed in the form:

$$E_{001} = \frac{6\sqrt{2}E_S I}{L^4\left(1 + 12\frac{I}{AL^2}\right)} \tag{2}$$

where E_S is the elastic modulus of the solid material, I is the moment of inertia of the beams along the axis of bending, L is the length of a single beam, and A is the

cross-sectional area of a single beam. In the case of both this investigation as well as the calculations by Zhu et al., the Kelvin cells are regular truncated octahedra, so all beams in the cell have the same length, cross-sectional area, and moment of inertia.

For the octet structure, deformation from loading along the z-axis of the cubic unit cell is dominated by the stretching of beams orthogonal to the load direction. The elastic modulus of this structure was described by Deshpande et al. in terms of the relative density of the lattice.[23] In this case, the stiffness of the octet-truss lattice along the (001) direction can be described using the equation:

$$E_{001} = \frac{\overline{\rho}}{5} E_S \tag{3}$$

where E_S is again the elastic modulus of the solid material and $\overline{\rho}$ is the relative density of the octet-truss material, which is described as follows:

$$\overline{\rho} = 6\sqrt{2}\pi \left(\frac{R}{L}\right)^2 \tag{4}$$

where R is the radius and L the length of a single beam.

Finally, for the design of the mixed structure, several considerations had to be made in its design in order to properly characterize its mechanical behavior. In order for a structure composed of a mixture of octet and Kelvin cells to be printed and reasonably characterized, the two different cells had to have the same unit cell size so they could be readily interchanged, as described in Table 1. Additionally, to minimize eccentric or non-uniform loading due to the arrangement of different cells in the mixed structure, the beams were printed such that the elastic modulus of both as-printed cells, Kelvin and octet, would be equivalent during uniaxial compression. Beam dimensions were established by equating the modulus descriptions of the Kelvin and octet designs to produce the relation:

$$\frac{4}{5}\left(\frac{L_k^4}{R_k^4} + 3\frac{L_k^2}{R_k^2}\right) = \left(\frac{L_o^2}{R_o^2}\right) \tag{5}$$

where L_k and R_k are the length and the radius of the beams in the Kelvin cells and L_o and R_o are the length and radius of the beams in the octet structure. This equation can be further simplified by relating the beam lengths between the two structures. Because the Kelvin and octet cells are both regular structures with equivalent unit cell sizes, some straightforward geometry shows that beams in the octet structure are

exactly twice the length of beams in the Kelvin structure, so $2L_k = L_o$. Substituting this into Equation 5 and simplifying produces the following relation.

$$\left(\frac{L_k^2}{R_k^2} + 3\right) = 5\left(\frac{R_k^2}{R_o^2}\right) \tag{6}$$

Based on this equation, for a chosen unit cell size and beam radius in one structure, the beam radius of the other structure will be fully defined under the constraint that both structures will have the same modulus. This relation was used to design all the mixed structures in this study and also motivated the beam dimensions for the individual octet and Kelvin cells that were investigated.

0.4 Results

0.4.1 Printing/Pyrolysis

As previously established, the material characteristics of the preceramic printing resin were previously investigated by Schmidt and Colombo.[1] Thermogravimetric analysis showing the total mass loss of the preceramic polymer as a function of temperature is shown in Figure 0.3.[1] After pyrolysis, the ceramic yield of 40.1 wt% is a weighted average of the ceramic yields of the pure RC 711: 7.4 wt%, and H44: 76.5 wt%, and is consistent with the expected value for the resin blend, confirming a homogeneous distribution of silicone chains from both compounds within the printed structure.[1]

To verify the amorphous character of the truss structures and confirm that truss designs and beam dimensions did not affect the crystallinity of the pyrolyzed SiOC, X-Ray diffraction was performed on pulverized truss structures of each design. The X-Ray diffraction patterns of all designs are shown in Figure 0.4. Regardless of truss design, all pyrolyzed SiOC structures showed complete amorphous character with no visible crystalline domains. It should be noted though, that the intensity counts are relatively low for these structures, which arises from the relatively low atomic number of all chemical constituents of SiOC.

In all Kelvin and octet structures, no sign of delamination or crack formation was visible in the as-printed state. Similarly, after pyrolysis, no cracks were observed in the produced SiOC structures, which are shown in Figure 0.5. Accurate copies of the designs (shown in Figures 0.1a and 0.1b) were produced with good shape retention and relatively isotropic body shrinkage (see Table 0.2).

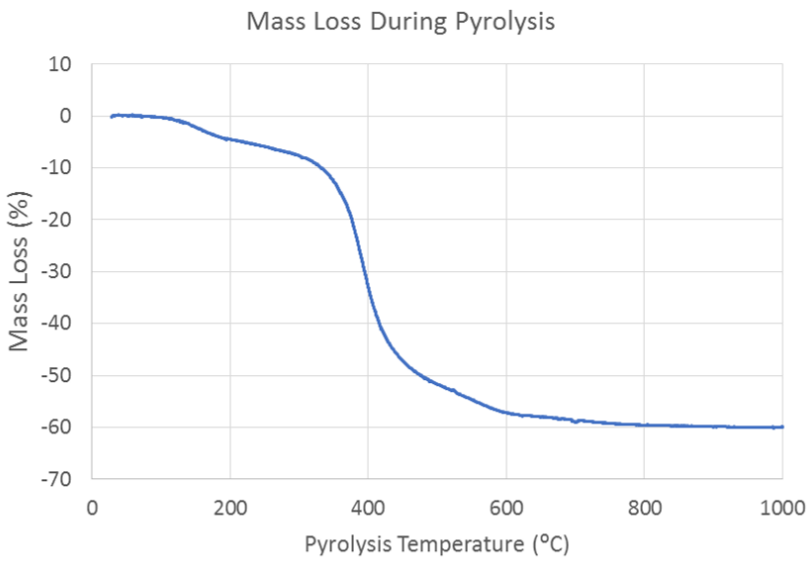

Figure 0.3: Thermogravimetric analysis showing the mass loss of the 50% RC 711 and 50% H44 preceramic polymer blend during pyrolysis as a function of heating temperature.

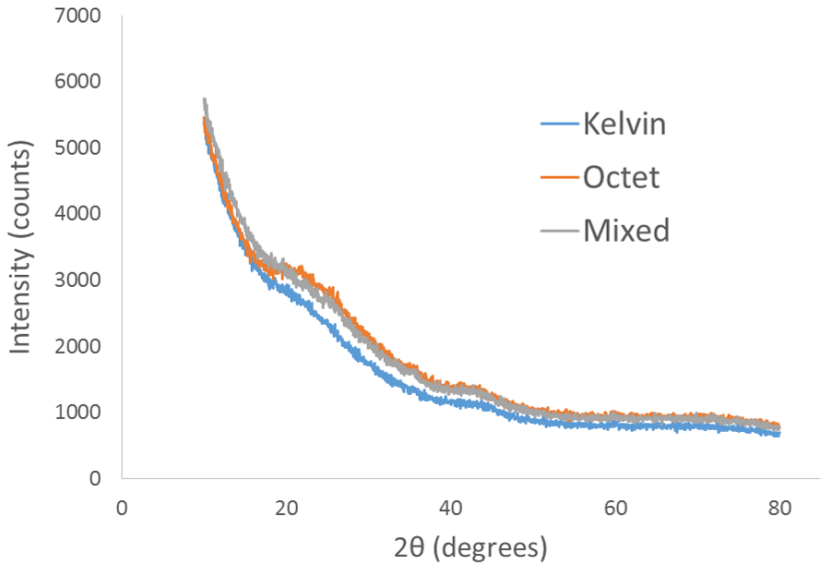

Figure 0.4: X-Ray diffraction analysis of the different truss structures, verifying uniform amorphous crystal structures across all three designs.

0.4.2 Shrinkage Measurements

The linear shrinkages of the overall structures as well as their constituent elements were investigated for the two Kelvin cell structures as well as for the octet structure, and comparisons of these are shown in Table 0.3. The aspect ratio reduction is also reported, which is the percentage change in the value of (L/D) for the beam elements

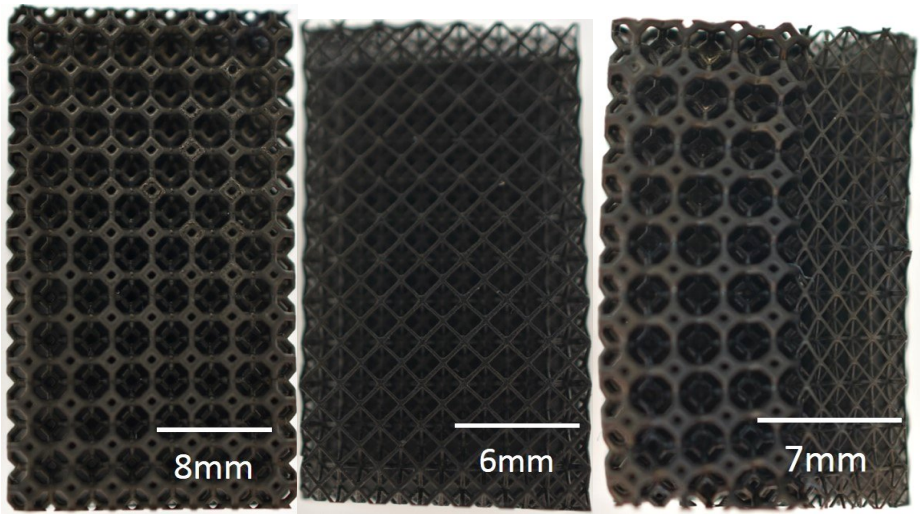

(a) Kelvin Structure (b) Octet Structure (c) Mixed Structure

Figure 0.5: Representative images of pyrolyzed and SiOC truss structures that have been prepared for uniaxial compression testing.

Table 0.2: Linear shrinkages of Kelvin and octet structures. Shrinkages measured based on total size of pyrolyzed specimens.

	Kelvin (Thin Beam)	Kelvin (Thick Beam)	Octet
X-Direction (%)	45.4 ± 1.6	43.7 ± 0.7	49.5 ± 1.4
Y-Direction (%)	44.8 ± 1.7	43.3 ± 0.8	48.8 ± 1.4
Z-Direction (%)	45.2 ± 0.8	43.4 ± 0.7	49.3 ± 1.3

in each structure, where L is beam length and D is beam diameter. Even though the linear shrinkages are isotropic for each structure, the shrinkages are not the same, neither within one structure nor between different structure geometries fabricated with the same material. Moreover, all beam elements show greater shrinkage in length than in diameter, and the shrinkage of the overall structure scales with a combination of the beam length shrinkage and the geometry of the beams within the structure.

The difference in overall shrinkage between the Kelvin and octet structures means that the mixed structure does not exhibit isotropic shrinkage, which is apparent in Figure 0.5c. All mixed structure specimens exhibited a slight curvature towards the octet section of the structure, which exhibited an overall linear shrinkage that was larger than that of the Kelvin structure by about 6%. Despite this nonuniform shrinkage, the mixed structures, like the Kelvin and octet structures, showed no

Table 0.3: Percent shrinkages of individual beam elements and beam aspect ratios (L/D) within each of the two truss structures. Average linear shrinkage of each truss structure is shown for comparison.

	Kelvin (Thin Beam)	Kelvin (Thick Beam)	Octet
Beam Diameter Shrinkage (%)	36.9 ± 1.7	37.5 ± 1.0	44.6 ± 1.3
Beam Length Shrinkage (%)	44.9 ± 1.6	42.0 ± 0.8	67.0 ± 1.0
Beam Volume Shrinkage (%)	77.9 ± 2.4	77.3 ± 0.7	90.0 ± 0.8
Aspect Ratio Reduction (%)	12.2 ± .01	14.8 ± .05	40.3 ± .01
Structure Average Shrinkage (%)	45.1 ± 1.4	43.5 ± 0.8	49.2 ± 1.4

cracks within the structure nor any sign of delamination or beam separation, even at the interface between the two geometrically different parts.

0.4.3 Truss Structure Response: Uniaxial Compression

Table 4 lists the porosity, strength and elastic modulus measured in uniaxial compression for all truss configurations. The thick beam Kelvin cell structure demonstrated an approximately 30% increase in failure strength over the thin beam Kelvin structure at the cost of only about 4% porosity. The octet structure exhibited a significantly larger porosity than any of the other structures as well as the lowest average strength and stiffness. Since the mixed structure is partially thick beam Kelvin design and partially octet design, its porosity and strength values lie between those of the octet and Kelvin structures. The elastic modulus of the mixed structure, however, is closer to that of the thick beam Kelvin structure.

Table 0.4: Comparison of the porosities and mechanical properties of the different truss designs characterized in this study.

	Kelvin (Thin Beam)	Kelvin (Thick Beam)	Octet	Mixed
Porosity (%)	85.3 ± 0.5	81.5 ± 1.2	91.1 ± 0.4	84.3 ± 0.1
Strength (MPa)	7.7 ± 1.1	10.0 ± 1.8	3.8 ± 0.7	9.4 ± 0.4
Elastic Modulus (GPa)	2.0 ± 0.7	3.1 ± 0.6	0.9 ± 0.1	2.7 ± 0.1

A representative stress-strain curve for each truss structure is shown in Figure 0.6. The stress-strain curves show the typical linear elastic behavior followed by brittle fracture of a ceramic material. Besides having several local failure events, especially in the octet samples, the structures exhibited linear load buildup and catastrophic failure after peak load was reached. After failure, the fracture behavior of the Kelvin,

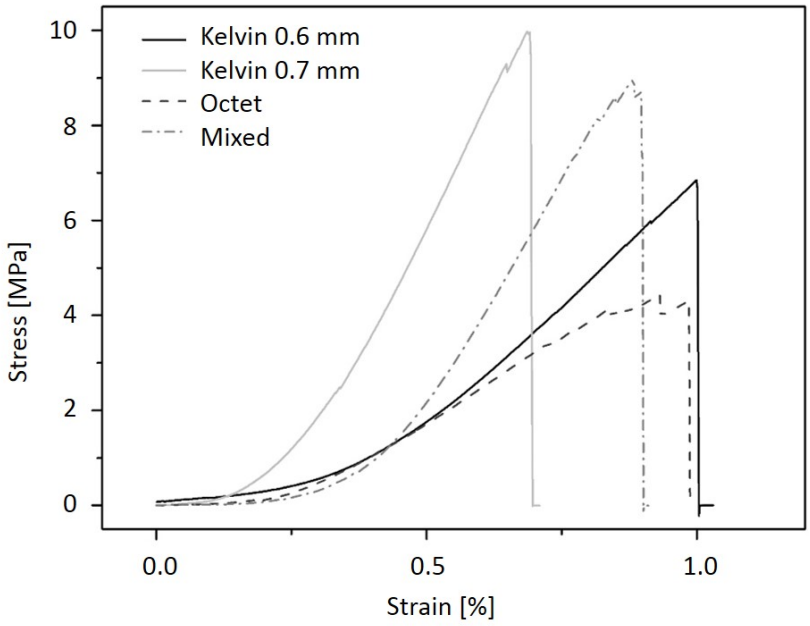

Figure 0.6: Representative uniaxial compression loading curves for each of the truss designs investigated in this study. Non-linearity at load onset is the result of spherical washer movement/alignment before load buildup.

octet, and mixed structure was analyzed using SEM fractography. Representative images of the observed fracture planes are shown in both low and high magnifications in Figure 0.7.

Fractography of all structures showed a dense SiOC material with no visible internal porosity (ρ = 2.1 g/cm^3). Though present, the individual print layers from the DLP printing process showed no influence on the fracture behavior, indicating that the failure strength between print layers was comparable to the strength within individual print layers and strong layer adhesion was achieved.

0.4.4 Beam Element Response: Flexure

The mean failure strengths, intercept failure strengths (63rd percentile), and Weibull Moduli of the individual beams in the structures are reported in Table 0.5. Two different kinds of fracture behavior were observed during the 3-point bending experiment (Figure 0.8). Figures 0.8c and 0.8f show cases of beam fracture where the nodes remain unaffected, whereas Figures 0.8b and 0.8e show beam failure where the node fractured and was partially removed with the beam. Failure both with and without node damage was observed, but no statistically significant difference in strength values was seen between the two fracture modes. The beams and cell nodes

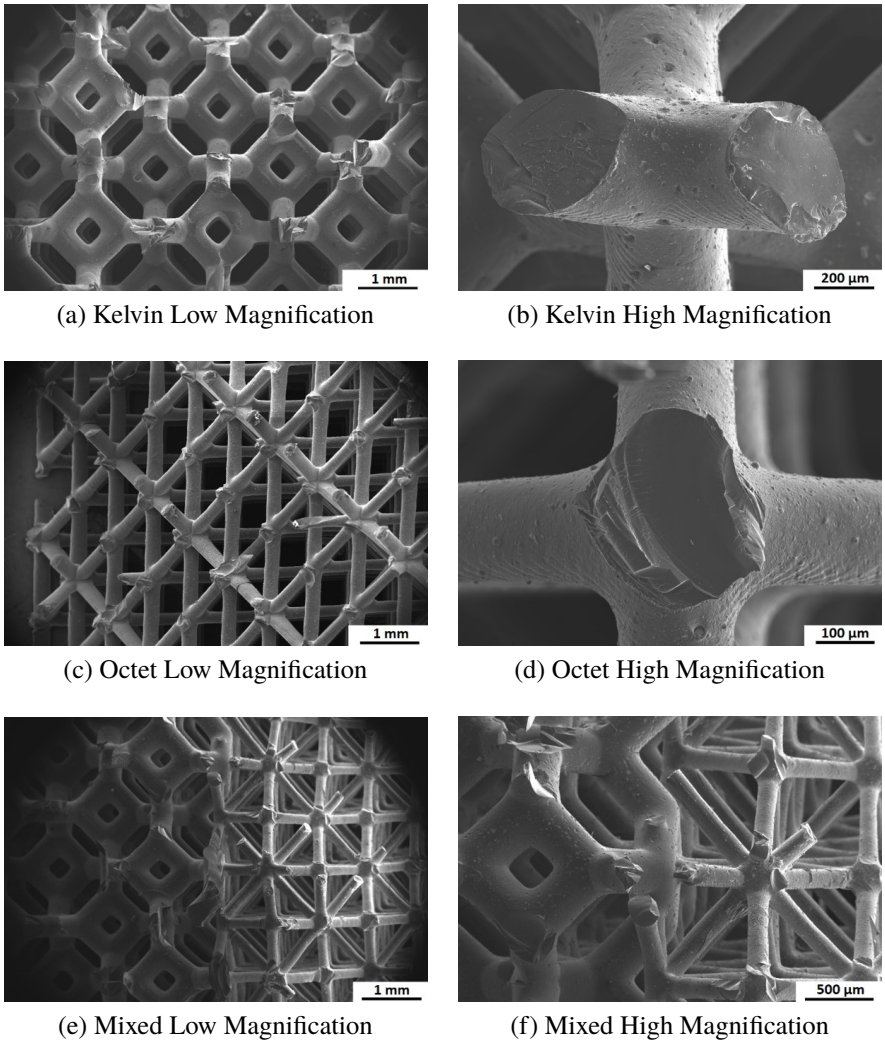

(a) Kelvin Low Magnification (b) Kelvin High Magnification

(c) Octet Low Magnification (d) Octet High Magnification

(e) Mixed Low Magnification (f) Mixed High Magnification

Figure 0.7: Low and high magnification fractography images showing the failure modes of each truss system in uniaxial compression.

adjacent to the loaded beams remain unaffected during the experiment, providing a rigid support of the tested beams.

0.5 Discussion

0.5.1 Deformation and Failure Modes

Before the mechanical responses of the ceramic structures can be properly discussed, it is critical to establish some of the principal factors that can influence truss strength and mechanical behavior. These can be separated into the categories of truss structure and porosity effects. The arrangement of beams in the truss structure dictates how the truss will deform under far-field loading, which ultimately impacts both the strength and stiffness of the structure. The truss arrangements in this study were chosen to

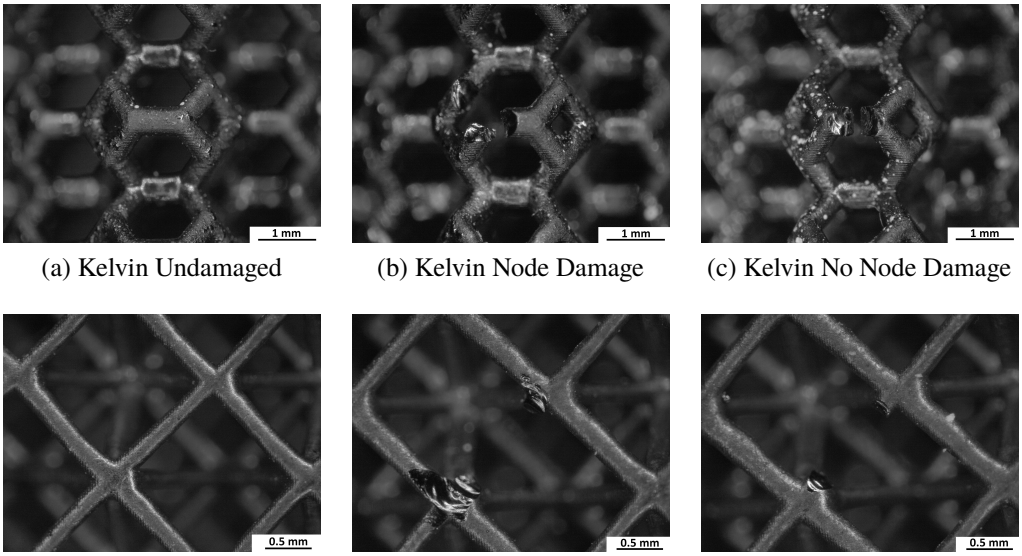

(a) Kelvin Undamaged (b) Kelvin Node Damage (c) Kelvin No Node Damage

(d) Octet Undamaged (e) Octet Node Damage (f) Octet No Node Damage

Figure 0.8: Fractography of beam pullout fracture in Kelvin and octet structures showing undamaged beams as well as pullout events with node damage and no node damage.

Table 0.5: Mean failure strengths, intercept failure strengths (63rd percentile) σ_0, and Weibull moduli of the beam elements of the Kelvin and octet truss designs. For each design, 10 beams were tested.

	Kelvin (Thin Beam)	Kelvin (Thick Beam)	Octet
Mean Failure Strength (GPa)	0.47 ± 0.16	0.54 ± 0.15	1.9 ± 0.27
σ_0 (GPa)	0.5	0.6	2.1
Weibull Modulus	3.0	3.9	8.5

exhibit different deformation modes, namely bending in the Kelvin structures and stretching in the octet structures. The effect of porosity in truss systems, on the other hand, is similar to that in foam structures or other porous media. Greater amounts of porosity lead to lower strengths due to the reduced amount of load bearing solid in the body.[24]

Firstly, to understand the effects of truss structure on deformation and failure, a fractography analysis was performed, shown in Figure 0.7. In the Kelvin structure, where deformation is dominated by bending of beam elements, the fracture path proceeds in the plane normal to the loading axis, although this fracture plane did have some curvature in certain specimens. The majority of beam failures in the Kelvin structures occurred in elements that were at a 45° angle with respect to the loading

axis, as these are the beams in bending when the structure is under compression. The majority of beams failed within the beam element near to a node, further indicating that the failure was ultimately flexural within each beam element.

The octet structure, which deforms by beam stretching, exhibited a markedly different behavior from the Kelvin structure. In all octet structures, failure occurred along a fracture plane at a 45° angle with respect to the loading direction. When considering the failure of individual beams, much of the fracture occurred in beams perpendicular to the loading direction, which were the elements in tension during loading of the structure. This also helps explain why global fracture of the specimen occurred along a 45° angle, as this the direction of nearest-neighbor tensile elements in the octet truss structure.

The mixed structure exhibited a combination of the fracture characteristics of both structures with respect to both fracture path and the orientation of fractured elements. The Kelvin section of the structure exhibited bending dominant failure with a fracture surface normal to the load axis and the octet section of the structure exhibited the same 45° angle failure path as the pure octet structure. The interface in the mixed structure proved to be robust, as the fracture path was not heavily influenced by the interface orientation. However, because failure was extremely rapid, it was not possible to determine whether failure events originated in the Kelvin structure or the octet structure, so the influence of deformation mode on failure behavior could not be properly evaluated.

0.5.2 Truss Structure Strength and Porosity

Figure 0.9 compares the strength versus the porosity on a logarithmic scale for all the lattice structures characterized in this study, and it indicates that although the strength of the octet structure is much lower than either of the Kelvin cell structures, its porosity is also significantly higher. Beyond this, there is insufficient data to establish clear relationships of the strength scaling of either structure.

When comparing to the mechanical strengths of other ceramic structures derived from preceramic polymers in literature, the strengths reported in this study are higher than those of SiOC structures produced by foaming or directional solidification,[25–27] but they are lower than those reported in Eckel et al.[5] for SiOC printed microlattices and honeycombs. It is suspected that much of the difference in the latter case is due to a combination of differences in truss geometry and drastic differences in specimen size and geometry, as most of the specimens tested in Eckel et al. were either of

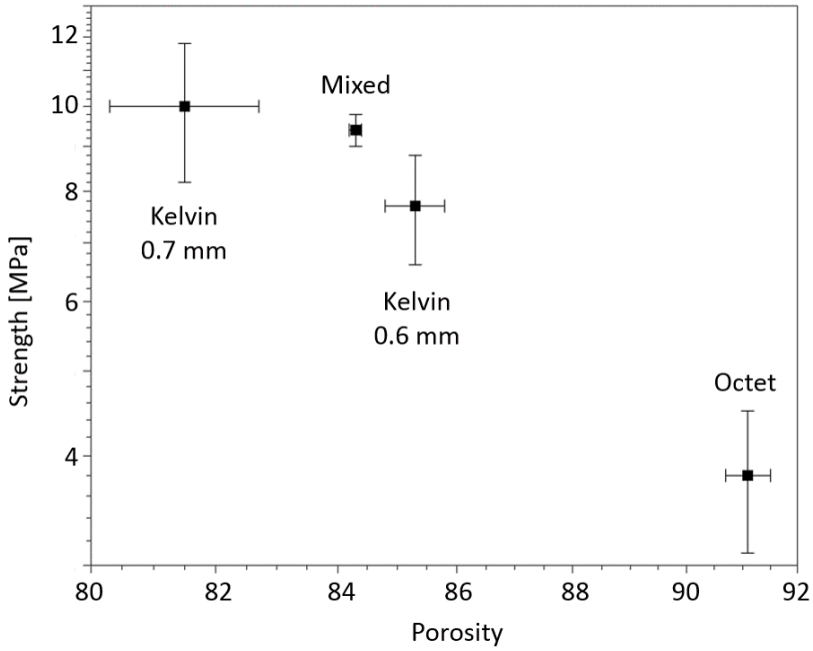

Figure 0.9: Comparison of strength and porosity between different truss designs. Both axes are plotted on a logarithmic scale.

relatively small volume or were sheets with single-cell thicknesses.

0.5.3 Effect of Shrinkage on Mechanical Response

It is apparent from the comparison in Figure 0.9 as well as Table 0.4 that the differences in mechanical response between the different structures are at least in part a result of different shrinkage behavior. In processes involving ceramic conversion, including additive manufacturing of ceramics, it is common to report linear shrinkage values in the x, y, and z-directions, or to report overall volume shrinkage, with focus being on whether this shinkage is isotropic or has a process-dependent directionality. Beyond this, the shrinkage of complex structures is typically only considered with respect to shape retention. Following this common trend, the linear shrinkage of the preceramic polymer blend used in this study was previously investigated on model cube structures, where it exhibited a homogeneous shrinkage of 51.5 ± 3.3 %.[1] However, a more detailed shrinkage analysis in this study found that while a representative structure can show uniform shrinkage in all directions, the constituent elements within these structures can each exhibit different shrinkage values, which change their geometry non-uniformly and lead to structure-dependent shrinkage.

Morphological analysis revealed that both Kelvin cell designs had similar structure

and beam element shrinkages despite having different beam diameters. In contrast, the octet design shrank around 6% more than the Kelvin ones, and also showed a remarkable difference in beam shrinkage with an additional decrease of 13% in beam volume, 7% in beam thickness, and more than 22% in length. The similar shrinkage characteristics between the Kelvin designs and the significant difference in the octet structure suggests that the shrinkage behavior depends on the geometric arrangement. It is possible that the architecture of the truss structure puts constraints on the material's ability to freely move during the transformation from preceramic polymer into ceramic material. This constrains the shrinkage that occurs as a result of the loss of mass during pyrolysis and densification. If the nodes are hypothesized as rigid points where the beams intersect and the contraction of beams is non-uniform, then the difference in geometrical arrangement of the nodes between the Kelvin and octet structures, will influence the free shrinkage movement of the individual beams, resulting in a different overall size change between the octet and Kelvin structures.

Table 0.3 indicates that in addition to producing structure dependent shrinkage, the pyrolysis process affected beams differently depending on their aspect ratio. The octet beams, which had a much higher aspect ratio (L/D), shrank in a manner that reduced their aspect ratio far more than any of the Kelvin beams. This suggests that during pyrolysis, the systems densifies and loses mass in a manner that minimizes the surface energy of the beams, thereby reducing the aspect ratio. This makes sense logically, as it is well understood that mass loss during pyrolysis is diffusion mediated, so size reduction would be dominated by minimum diffusion distances. However, to properly characterize diffusion-dependent shrinkage, the diffusivities of the volatile species in the preceramic polymer would have to be measured, and this is both nontrivial and beyond the scope of this study.

Despite the difference seen in unit cell shrinkage between structures, the overall shrinkages of both Kelvin and octet structures are uniform in every direction and therefore globally isotropic. This is not the case in the mixed structure, where the Kelvin and octet parts are both present, leading to non-homogeneous shrinkage. This demonstrates that even though a structure consisting of two different geometrical arrangements can be produced via additive manufacturing, special attention must be placed on the shrinkage analysis of the constituent elements, which will not necessarily match the shrinkage of representative solid bodies. Similar anisotropic shrinkage effects may also be present in ceramic additive manufacturing processes that involve a sintering step instead of a pyrolysis step, but this has been given

little research attention to date. In the case of preceramic systems however, it has been demonstrated here that the shrinkage behavior of a constrained net-shape part produced via stereolithography is nontrivial, and this shrinkage must be thoroughly investigated in order for additive manufacturing to be viable for the production of complex ceramic parts for technical applications.

0.5.4 Beam Element Strength

The strengths of individual beam elements were investigated in this study using a testing method developed based on the work of Brezny et al.[20] When compared to the strengths of the overall truss structures, the flexural strengths of the individual beams show a markedly different trend. Despite having different structure strengths, the two Kelvin structures investigated in this study do not have individual beam strengths that are different with statistical significance. The octet structure however, which had the lowest strength of any of the truss structures investigated in this study, had beam strengths that were about four times stronger than the Kelvin beams. This difference is likely due to size effects, which can be described using the conventional weakest link model. For surface dominant flaws, this effect can be quantified using the following comparison [28]:

$$\frac{\overline{\sigma}_{\mathrm{max1}}}{\overline{\sigma}_{\mathrm{max2}}} = \left(\frac{k_2 A_2}{k_1 A_1}\right)^{\frac{1}{m}} \tag{7}$$

where 1 and 2 are the different surface areas being compared, $\overline{\sigma}_{max}$ is the maximum stress in the given beam geometry, m is the Weibull modulus of the solid material, A is the beam surface area (excluding faces in contact with nodes), and k is a loading factor that changes depending on the cross section and aspect ratio of the beam being bent. Using both the post-pyrolysis beam dimensions and the average Weibull modulus value from Table 0.5 in Equation 7 indicates that the strength of the octet structure should be about twice that of the Kelvin structures, which explains much of the discrepancy seen between the two systems.

Size effects can explain much of the difference in behavior between the octet and Kelvin beam elements, but not why the more slender Kelvin beams do not perform better than the thicker ones. One possible reason for this is that the effect of added beam thickness did more to improve the bending strength than the increase in volume did to reduce it. It is also possible that the lower aspect ratio of the Kelvin beams distorted the bending behavior, making the effect of volume on failure strength less apparent. Additionally, it should be noted that although the individual octet beams

were extremely strong, the octet structure itself demonstrated the lowest strength of all structures tested in this study. This is a testament to the fact that weakest link behavior is governed by volume or area rather than characteristic length. Regardless of how slender the beams are, as more are introduced, the total volume and surface area of structure increase, which raises the probability of a large flaw being present in a single beam, which will ultimately lead to a reduction of strength. This effect, while simple, is less from an experimental standpoint, as beams with larger flaws would likely not be viable as standalone bodies, but could easily be part of larger truss structure, where they would greatly reduce overall strength. This subtle effect shows that even in complex architected structures, strength is still governed by the principal phenomena of porosity and geometry of the solid body.

0.5.5 Evaluation of Structure Elastic Modulus

For the Kelvin cell structures, the derivation from Zhu et al. (shown earlier in Equation 2) describes what the elastic modulus of the truss structure should be with respect to the elastic modulus of the solid material for a given beam length and radius.[22] Since all the truss structures in this study were fabricated with the same preceramic polymer blend and pyrolysis process, it is reasonable to assume that the elastic modulus of the solid SiOC ceramic is the same across all structures. This was verified through nanoindentation, and the elastic modulus of the SiOC for both the Kelvin and octet structures was found to be about 65 GPa. With this assumption and the beam dimensions measured in the shrinkage analysis, it is possible to determine the expected stiffness ratios across different structures using the following form:

$$\text{StiffnessRatio} = \frac{E_{001}^{\text{Design2}}}{E_{001}^{\text{Design1}}} \tag{8}$$

For the Kelvin structures, the expected stiffness ratio between designs is that the thick beam Kelvin structure would be about twice as stiff as the thin beam Kelvin structure, but the experimental results show a ratio of about 1.5 instead. This difference is likely due to the relatively low aspect ratio of the beams in the Kelvin structures tested in this study. A print design intended to produce a high bending stiffness alongside anisotropic beam shrinkage during pyrolysis resulted in Kelvin cell beams that had aspect ratios on the order of 2:1, whereas the analytical calculation of stiffness uses the assumption of more slender beams, typically on the order of at least 5:1. This lack of slenderness would cause some of the stiffness of the Kelvin cells to be due to the deformation of the nodes, which would cause a more complex deformation behavior

that deviates from the predictions established by Zhu et al.[22] using traditional beam theory. A more detailed discussion of the role of the nodes in truss structures composed of non-slender beams is discussed in Portela et al.[29]

While a lack of slenderness in beams provides a plausible explanation for the difference in stiffness ratio between the two Kelvin structures, it does not adequately explain the stiffness of the octet structures in any way. If both designs were printed to be of equal elastic modulus, based on the calculations by Deshpande et al. (shown in Equations 3 and 4), it would be expected that the octet structure would exhibit higher stiffness than either of the Kelvin structures due to the dramatic reduction in beam length during pyrolysis, which is not the case. This observation, in combination with the difference in strength between the individual octet beams and the octet structure further indicates that some eccentricity of loading may have occurred during compression, which would affect the deformation mode of the octet beams.

In the case of the mixed structures, even though shrinkage was uneven and load eccentricity is expected, a relative analysis of the expected stiffness can still be performed. Since the mixed structure is an isostrain configuration of the thick beam Kelvin and octet structures we can use the experimental modulus measurements for each of these structures along with a rule of mixtures calculation to determine the modulus of the mixed structure

$$E_{mixed} = v_{Kelvin}E_{Kelvin} + v_{octet}E_{octet} \tag{9}$$

where $v_{Kelvin} = \frac{4}{7}$ is the volume fraction of Kelvin cells in the mixed structure and $v_{octet} = \frac{3}{7}$ is the volume fraction of octet cells in the mixed structure. This calculation predicts an elastic modulus for the mixed structure of about 2.2 GPa, which is slightly lower than the measured 2.7 GPa. The non-uniform shrinkage of the mixed structures would make the effective fraction of Kelvin structure larger than predicted from as-printed geometries, which would result in an increase in elastic modulus. Additionally, the curvature of the mixed structure would make the load bearing portion of the octet structure even smaller, further increasing the influence of the Kelvin structure on the elastic modulus.

0.5.6 Potential for Mixed Structures

Although the mixed structures in this study had load eccentricity and bending due to non-uniform shrinkage during pyrolysis, it is still worthwhile to assess the potential implications for these types of mixed structures. Previously, many different truss

systems have been designed to create bulk structures with a variety of different mechanical, optical, or acoustic properties. Often referred to as metamaterials, these types of structures can be designed to have properties that normal solids cannot exhibit, such as high acoustic dampening, negative coefficients of thermal expansion, or nonuniform mechanical response, as outlined in reviews by Deshpande et al. and Wegener et al.[30, 31] Experimentally, many different trusses have been fabricated using additive manufacturing techniques such as 3D printing, but mechanical characterization of these structures has generally been limited to the elastic regime, with almost no consideration of failure mechanisms.[30–33]

However, ceramic truss structures present an interesting opportunity mechanically as materials with designed anisotropic structure, as the only mechanical responses they tend to exhibit are elastic deformation and brittle fracture. If one could design a ceramic truss system composed of compatible truss structures with different deformation modes but identical elastic moduli, it could in theory produce a structure with uniform bulk elastic properties but very controlled and specified failure. Due to differences in beam deformation behavior, it would be expected that, despite having identical stiffnesses, one truss structure in this mixed material would have a lower failure strength than the other, which would mean that when the bulk structure was loaded, the cells of the weaker structure would fail preferentially. In experimental practice, this behavior would even be expected in the case of different structures in parallel. If both truss elements have the same stiffness, and are loaded in parallel, it would be expected that the elements with lower strength would fail first, and fracture behavior would be dictated the location and distribution of the lower strength truss elements. However, in this study, failure in mixed structures was too rapid for the origin of failure to be characterized. While the idea of pairing compatible truss designs to tailor elastic deformation has been explored previously, using differences in deformation modes to drive and control failure in trusses has to date not been well investigated.[18] A design of this type would allow for predictable and potentially controllable failure properties at the bulk scale, which could have a variety of applications both in fracture research as well as in industry, where predictable failure can be used to mitigate loss of functionality.

0.6 Summary

To study the influence of complex geometry on the mechanical properties of printed ceramics as well as explore the potential for designed structures as a mechanism to control failure behavior, four different truss systems were printed using DLP of

preceramic polymer resin. Two of the truss designs were Kelvin cell arrangements which deform by bending of beams, one design was an octet cell arrangement which deforms by stretching of beams, and one design was a mixture of the two in parallel. The designs were characterized both at the structure level through uniaxial compression and at the beam element level using a previously established strut flexure method. Mechanical analysis of the truss structures after pyroylysis revealed that each of the different designs had different strength, stiffness, and shrinkage, despite attempts to control both their size and stiffness based on uniform linear shrinkage assumptions established from prior studies of printed preceramic polymer. Fractographic analyses of each design indicated that failure occurred as expected given the dominant beam loading regimes. The different structure strengths could reasonably be attributed to different porosities, but the relatively low stiffness and strength of the octet design in comparison to theory indicated that some amount of bending in the structure due to load eccentricity may have occurred. Analysis of the individual beam elements showed a reverse trend from the structures, with the individual elements of the octet beams being about four times stronger than those of the individual Kelvin beams. Much of this difference in strength was attributable to size effects arising from the dramatically reduced surface area the octet beam elements compared to the Kelvin ones. However, the difference in measured strength between the octet structure and its individual beam elements highlights some of the challenges that can arise when relying on the assumption that a structure built from strong individual elements will itself be strong. Furthermore, this study shows that when fabricating complex geometries, careful consideration must be given to the structure-dependent shrinkage behavior of additively manufactured ceramics. The current standards of linear shrinkage and mass loss analysis fail to capture these shrinkage effects. If additive manufacturing of ceramics is to be viable for industrial applications, it is critical to understand these shrinkage behaviors, which will require investigations well beyond those of simple representative bodies. However, if this degree of shrinkage control can be achieved, there is potential to create truss structures with uniform elastic behavior and failure mechanisms that are controlled solely through designed variations in failure strength.

REFERENCES

[1] Johanna Schmidt and Paolo Colombo. Digital light processing of ceramic components from polysiloxanes. *Journal of the European Ceramic Society*, 38(1):57–66, jan 2018. ISSN 0955-2219. doi: 10.1016/J.JEURCERAMSOC.2017.07.033.

[2] J. W. Obreimoff. The Splitting Strength of Mica. *Proceedings of the Royal Society of London A*, 25:290–297, 1930. ISSN 1364-5021. doi: 10.1098/rspa.1933.0074.

[3] Brian R. Lawn. *Fracture of brittle solids*. Cambridge University Press, 1993. ISBN 9780511623127.

[4] Paolo Colombo, Johanna Schmidt, Giorgia Franchin, Andrea Zocca, and Jens Günster. Additive manufacturing techniques for fabricating complex ceramic components from preceramic polymers. *American Ceramic Society Bulletin*, pages 16–24, 2017.

[5] Zak C Eckel, Chaoyin Zhou, John H Martin, Alan J Jacobsen, William B Carter, and Tobias A Schaedler. Additive manufacturing of polymer-derived ceramics. *Science (New York, N.Y.)*, 351(6268):58–62, jan 2016. ISSN 1095-9203. doi: 10.1126/science.aad2688.

[6] Y. de Hazan and D. Penner. SiC and SiOC ceramic articles produced by stereolithography of acrylate modified polycarbosilane systems. *Journal of the European Ceramic Society*, 37(16):5205–5212, dec 2017. ISSN 0955-2219. doi: 10.1016/J.JEURCERAMSOC.2017.03.021.

[7] Erika Zanchetta, Marco Cattaldo, Giorgia Franchin, Martin Schwentenwein, Johannes Homa, Giovanna Brusatin, and Paolo Colombo. Stereolithography of SiOC Ceramic Microcomponents. *Advanced Materials*, 28(2):370–376, jan 2016. ISSN 09359648. doi: 10.1002/adma.201503470.

[8] T.-A. Pham, D.-P. Kim, T.-W. Lim, S.-H. Park, D.-Y. Yang, and K.-S. Lee. Three-Dimensional SiCN Ceramic Microstructures via Nano-Stereolithography of Inorganic Polymer Photoresists. *Advanced Functional Materials*, 16(9): 1235–1241, jun 2006. ISSN 1616-301X. doi: 10.1002/adfm.200600009. URL http://doi.wiley.com/10.1002/adfm.200600009.

[9] Andrea Zocca, Cynthia M. Gomes, Andreas Staude, Enrico Bernardo, Jens Günster, and Paolo Colombo. SiOC ceramics with ordered porosity by 3D-printing of a preceramic polymer. *Journal of Materials Research*, 28 (17):2243–2252, sep 2013. ISSN 0884-2914. doi: 10.1557/jmr.2013.129. URL https://www.cambridge.org/core/product/identifier/S0884291413001295/type/journal{_}article.

[10] Giorgia Franchin, Larissa Wahl, and Paolo Colombo. Direct ink writing of ceramic matrix composite structures. *Journal of the American Ceramic Society*, 100(10):4397–4401, oct 2017. ISSN 00027820. doi: 10.1111/jace.15045. URL http://doi.wiley.com/10.1111/jace.15045.

[11] Laura Brigo, Johanna Eva Maria Schmidt, Alessandro Gandin, Niccolò Michieli, Paolo Colombo, and Giovanna Brusatin. 3D Nanofabrication of SiOC Ceramic Structures. *Advanced Science*, 5(12):1800937, dec 2018. ISSN 21983844. doi: 10.1002/advs.201800937. URL http://doi.wiley.com/10.1002/advs.201800937.

[12] Xifan Wang, Franziska Schmidt, Dorian Hanaor, Paul H. Kamm, Shuang Li, and Aleksander Gurlo. Additive manufacturing of ceramics from preceramic polymers: A versatile stereolithographic approach assisted by thiol-ene click chemistry. *Additive Manufacturing*, 27:80–90, may 2019. ISSN 2214-8604. doi: 10.1016/J.ADDMA.2019.02.012. URL https://www.sciencedirect.com/science/article/pii/S2214860418310479.

[13] Giorgia Franchin, Halide Maden, Larissa Wahl, Andrea Baliello, Marco Pasetto, Paolo Colombo, Giorgia Franchin, Halide Selin Maden, Larissa Wahl, Andrea Baliello, Marco Pasetto, and Paolo Colombo. Optimization and Characterization of Preceramic Inks for Direct Ink Writing of Ceramic Matrix Composite Structures. *Materials*, 11(4):515, mar 2018. ISSN 1996-1944. doi: 10.3390/ma11040515. URL http://www.mdpi.com/1996-1944/11/4/515.

[14] Andrea Zocca, Giorgia Franchin, Hamada Elsayed, Emilia Gioffredi, Enrico Bernardo, and Paolo Colombo. Direct Ink Writing of a Preceramic Polymer and Fillers to Produce Hardystonite (Ca ₂ ZnSi ₂ O ₇) Bioceramic Scaffolds. *Journal of the American Ceramic Society*, 99(6):1960–1967, jun 2016. ISSN 00027820. doi: 10.1111/jace.14213. URL http://doi.wiley.com/10.1111/jace.14213.

[15] Giovanni Pierin, Chiara Grotta, Paolo Colombo, and Cecilia Mattevi. Direct Ink Writing of micrometric SiOC ceramic structures using a preceramic polymer. *Journal of the European Ceramic Society*, 36(7):1589–1594, jun 2016. ISSN 0955-2219. doi: 10.1016/J.JEURCERAMSOC.2016.01.047. URL https://www.sciencedirect.com/science/article/abs/pii/S0955221916300474.

[16] A Zocca, H Elsayed, E Bernardo, C M Gomes, M A Lopez-Heredia, C Knabe, P Colombo, and J Günster. 3D-printed silicate porous bioceramics using a non-sacrificial preceramic polymer binder. *Biofabrication*, 7(2):025008, may 2015. ISSN 1758-5090. doi: 10.1088/1758-5090/7/2/025008. URL http://stacks.iop.org/1758-5090/7/i=2/a=025008?key=crossref.ad6c583046cb0f2af81ab1c2c8b34a48.

[17] Tiemo Bückmann, Nicolas Stenger, Muamer Kadic, Johannes Kaschke, Andreas Frölich, Tobias Kennerknecht, Christoph Eberl, Michael Thiel, and Martin Wegener. Tailored 3D mechanical metamaterials made by dip-in direct-laser-writing optical lithography. *Advanced Materials*, 24(20):2710–2714, 2012. ISSN 09359648. doi: 10.1002/adma.201200584.

[18] Julian Panetta, Qingnan Zhou, Luigi Malomo, Nico Pietroni, Paolo Cignoni, and Denis Zorin. Elastic textures for additive fabrication. *ACM Transactions on Graphics*, 34(4):1–12, jul 2015. ISSN 07300301. doi: 10.1145/2766937. URL http://dl.acm.org/citation.cfm?doid=2809654.2766937.

[19] Caroline A Schneider, Wayne S Rasband, and Kevin W Eliceiri. NIH Image to ImageJ: 25 years of image analysis. *Nature Methods*, 9(7):671–675, jul 2012. ISSN 1548-7091. doi: 10.1038/nmeth.2089. URL http://www.nature.com/articles/nmeth.2089.

[20] Rasto Brezny, David J. Green, and Chuong Quang Dam. Evaluation of Strut Strength in Open-Cell Ceramics. *Journal of the American Ceramic Society*, 72(6):885–889, jun 1989. ISSN 0002-7820. doi: 10.1111/j.1151-2916.1989.tb06239.x.

[21] ASTM C1684 - 18, Standard Test Method for Flexural Strength of Advanced Ceramics at Ambient Temperature Cylindrical Rod Strength, 2018.

[22] H.X. Zhu, J.F. Knott, and N.J. Mills. Analysis of the elastic properties of open-cell foams with tetrakaidecahedral cells. *Journal of the Mechanics and Physics of Solids*, 45(3):319–343, mar 1997. ISSN 0022-5096. doi: 10.1016/S0022-5096(96)00090-7.

[23] V.S. Deshpande, N.A. Fleck, and M.F. Ashby. Effective properties of the octet-truss lattice material. *Journal of the Mechanics and Physics of Solids*, 49 (8):1747–1769, aug 2001. ISSN 0022-5096.

[24] Lorna J Gibson and Michael F Ashby. *Cellular Solids: Structure and Properties - Lorna J. Gibson, Michael F. Ashby - Google Books*. Cambridge University Press, 2 edition, 1997. ISBN 0 521 49911 9.

[25] Paolo Colombo, John R. Hellmann, and David L. Shelleman. Thermal Shock Behavior of Silicon Oxycarbide Foams. *Journal of the American Ceramic Society*, 85(9):2306–2312, sep 2002. ISSN 0002-7820. doi: 10.1111/j.1151-2916.2002.tb00452.x.

[26] Cekdar Vakifahmetoglu, Paolo Colombo, Alberto Pauletti, Cristina Fernandez Martin, and Florence Babonneau. SiOC Ceramic Monoliths with Hierarchical Porosity. *International Journal of Applied Ceramic Technology*, 7(4):528–535, mar 2009. ISSN 1546542X. doi: 10.1111/j.1744-7402.2009.02365.x. URL http://doi.wiley.com/10.1111/j.1744-7402.2009.02365.x.

[27] Noriaki Arai and Katherine T. Faber. Hierarchical porous ceramics via two-stage freeze casting of preceramic polymers. *Scripta Materialia*, 162:72–76, mar 2019. ISSN 1359-6462. doi: 10.1016/J.SCRIPTAMAT.2018.10.037. URL https://www.sciencedirect.com/science/article/pii/S1359646218306663.

[28] J. B. Wachtman, W. Roger. Cannon, and M. John. Matthewson. *Mechanical properties of ceramics*. Wiley, 2009. ISBN 9780470451502. URL https://www.wiley.com/en-us/Mechanical+Properties+of+Ceramics{\%}2C+2nd+Edition-p-9780470451502.

[29] Carlos M. Portela, Julia R. Greer, and Dennis M. Kochmann. Impact of node geometry on the effective stiffness of non-slender three-dimensional truss lattice architectures. *Extreme Mechanics Letters*, 22:138–148, jul 2018. ISSN 2352-4316. doi: 10.1016/J.EML.2018.06.004. URL https://www.sciencedirect.com/science/article/pii/S2352431618300725.

[30] N. A. Fleck, V. S. Deshpande, and M. F. Ashby. Micro-architectured materials: past, present and future. *Proceedings of the Royal Society A: Mathematical, Physical and Engineering Sciences*, 466(2121):2495–2516, sep 2010. ISSN 1364-5021. doi: 10.1098/rspa.2010.0215. URL http://www.royalsocietypublishing.org/doi/10.1098/rspa.2010.0215.

[31] Johan Christensen, Muamer Kadic, Oliver Kraft, and Martin Wegener. Vibrant times for mechanical metamaterials. *MRS Communications*, 5(03):453–462, sep 2015. ISSN 2159-6859. doi: 10.1557/mrc.2015.51. URL http://www.journals.cambridge.org/abstract{_}S2159685915000518.

[32] T A Schaedler, A J Jacobsen, A Torrents, A E Sorensen, J Lian, J R Greer, L Valdevit, and W B Carter. Ultralight metallic microlattices. *Science (New York, N.Y.)*, 334(6058):962–965, nov 2011. ISSN 1095-9203. doi: 10.1126/science.1211649. URL http://www.ncbi.nlm.nih.gov/pubmed/22096194.

[33] Lucas R. Meza, Satyajit Das, and Julia R. Greer. Strong, lightweight, and recoverable three-dimensional ceramic nanolattices. *Science*, 345(6202):1322–1326, sep 2014. ISSN 0036-8075. doi: 10.1126/SCIENCE.1255908. URL http://science.sciencemag.org/content/345/6202/1322.